NeuroImage 102 (2014) 393–406

Contents lists available at ScienceDirect

NeuroImage

journal homepage: www.elsevier.com/locate/ynimg

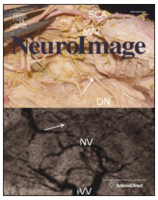

Optical Coherence Tomography angiography reveals laminar microvascular hemodynamics in the rat somatosensory cortex during activation

Vivek J. Srinivasan *, Harsha Radhakrishnan

Department of Biomedical Engineering, University of California at Davis, 451 E. Health Sciences Dr. GBSF 2303, Davis, CA 95616, USA

ARTICLE INFO

Article history:
Accepted 2 August 2014
Available online 8 August 2014

Keywords:
Neurovascular coupling
Optical Coherence Tomography
Three-dimensional microscopy
Somatosensory cortex
Hemodynamics
Scattering
Forepaw
Laminar
functional Magnetic Resonance Imaging
Blood-oxygen-level-dependent
Hematocrit
Blood volume

ABSTRACT

The BOLD (blood-oxygen-level dependent) fMRI (functional Magnetic Resonance Imaging) signal is shaped, in part, by changes in red blood cell (RBC) content and flow across vascular compartments over time. These complex dynamics have been challenging to characterize directly due to a lack of appropriate imaging modalities. In this study, making use of infrared light scattering from RBCs, depth-resolved Optical Coherence Tomography (OCT) angiography was applied to image laminar functional hyperemia in the rat somatosensory cortex. After defining and validating depth-specific metrics for changes in RBC content and speed, laminar hemodynamic responses in microvasculature up to cortical depths of >1 mm were measured during a forepaw stimulus. The results provide a comprehensive picture of when and where changes in RBC content and speed occur during and immediately following cortical activation. In summary, the earliest and largest microvascular RBC content changes occurred in the middle cortical layers, while post-stimulus undershoots were most prominent superficially. These laminar variations in positive and negative responses paralleled known distributions of excitatory and inhibitory synapses, suggesting neuronal underpinnings. Additionally, the RBC speed response consistently returned to baseline more promptly than RBC content after the stimulus across cortical layers, supporting a "flow-volume mismatch" of hemodynamic origin.

Introduction

The BOLD (blood-oxygen-level dependent) fMRI (functional Magnetic Resonance Imaging) (Kwong et al., 1992; Ogawa et al., 1992) signal results from complex blood flow, blood volume, and oxygen consumption changes during a period of increased neuronal activation (Mandeville et al., 1999). Characterization of the precise spatiotemporal sequence of hemodynamic events that accompanies neuronal activation is essential to the interpretation of BOLD fMRI as well as other macroscopic neuroimaging signals (Raichle and Mintun, 2006). In particular, as field strengths and resolutions improve, the question of what "neuronal specificity" is afforded by the BOLD fMRI signal remains open. Related to this question is the extent to which salient response features such as laminar BOLD (Lau et al., 2011; Logothetis et al., 2002; Siero et al., 2011; Silva and Koretsky, 2002; Yu et al., 2014), negative BOLD (Shmuel et al., 2002), the initial dip (Buxton, 2001), and the post-stimulus undershoot (Chen and Pike, 2009) are actuated directly by neuronal activity.

A variety of imaging techniques have been used to understand the underpinnings of the fMRI BOLD response. The BOLD signal itself offers clues to its own origins as a "washout" phenomenon; it typically originates earliest in the middle cortical layer microvasculature (Yu et al., 2012), corresponding to cortical inputs (Yu et al., 2014), while the largest and most delayed signal is found in draining veins (Goense and Logothetis, 2006). However, drawing inferences about neuronal activity from the amplitude and timing of the BOLD signal requires accounting for flow and volume changes that can impact the BOLD signal. Therefore, MR methods (Mandeville et al., 1998) have been applied to characterize plasma volume (Harel et al., 2006; Lu et al., 2004; Mandeville and Marota, 1999; Shen et al., 2008; Shih et al., 2013; Smirnakis et al., 2007; Zhao et al., 2006) and flow (Jin and Kim, 2008). These studies typically show laminar activation patterns peaking in the middle cortical layers, and possible laminar post-stimulus undershoot patterns (Yacoub et al., 2006). Optical Intrinsic Signal Imaging (OISI), based on hemoglobin absorption, has enabled low-resolution two-dimensional surface mapping, suggesting arteriolar control of the early hemodynamic response (Vanzetta et al., 2005). However, intrinsic absorption imaging does not enable depth resolution and hence cannot distinguish cortical laminae (however see Hillman et al., 2007). Two-photon microscopy diameter measurements have enabled exquisite compartment-specific (Drew et al., 2011) and depth-resolved (Tian

---

* Corresponding author at: Department of Biomedical Engineering, University of California at Davis, 451 E Health Sciences Dr GBSF 2521, Davis CA 95616.
E-mail address: vjsriniv@ucdavis.edu (V.J. Srinivasan).

http://dx.doi.org/10.1016/j.neuroimage.2014.08.004
1053-8119/

et al., 2010) quantification of vascular volume changes, demonstrating laminar differences in arteriolar dilation that parallel BOLD onset times up to superficial layer IV (Tian et al., 2010).

Red blood cells are the principal oxygen carriers in blood. As such, they directly impact the BOLD response. Therefore characterizing red blood cell content and flow changes in space and time is of critical importance in explaining BOLD. Two-photon microscopy diameter (Tian et al., 2010) and MR plasma volume (Mandeville et al., 1998) measurements share the limitation that they can only assess red blood cell content if assumptions are made about hematocrit. While mass conservation must hold and average hematocrit should remain constant over large volumes (Herman et al., 2009), it remains unclear to what extent this remains true transiently within compartments over small activation volumes. Indeed, localized transient compartment-specific hematocrit changes during activation have been suggested (Hillman et al., 2007). While red blood cell density measurements are possible with two-photon microscopy, measurements remain challenging and unclear responses are typically observed near the cortical surface during activation (Kleinfeld et al., 1998; Stefanovic et al., 2008). Moreover, for 700–900 nm excitation wavelengths, two-photon microscopy does not penetrate to the deeper cortical layers IV–V that show the largest hemodynamic changes in fMRI in rodents. Thus, a highly specific method of measuring red blood cell changes across cortical depths with micron-scale resolution remains elusive.

Here, we use spectral/Fourier domain Optical Coherence Tomography (OCT) angiography (Radhakrishnan and Srinivasan, 2013) at 1300 nm to investigate the laminar hemodynamic response to functional activation in the rat somatosensory cortex, at depths of > 1 mm. We focus on the following questions: What are the amplitudes and kinetics of microvascular RBC content changes during functional activation in the cortex? What is the temporal relationship between microvascular RBC content and speed? To answer these questions, we use the fact that red blood cell backscattering is an intrinsic indicator of quantity over a physiological range of hematocrits. We then validate techniques to estimate the amount of RBC backscattering without oximetric confounds and apply these methodologies in vivo.

Our results have led to a number of new findings. The earliest and largest RBC content increase occurred in the middle cortical layers, while the most prominent undershoots occurred superficially. The large RBC content increases in the middle cortical layers, taken together with plasma-tracer based fMRI results from other studies, imply prominent microvascular dilation in the middle cortical layers. The more prominent superficial undershoots agree with the large fraction of inhibitory GABA neurons in layers I–III (Avermann et al., 2012) and their postulated role in vasoconstriction (Cauli et al., 2004). Finally, RBC speed changes paralleled those in RBC content, but with a consistent time lag in the return to baseline across layers, suggesting a “flow-volume mismatch” and delayed washout of RBCs.

Methods

Optical Coherence Tomography (Huang et al., 1991) is the optical analog of ultrasound, and generates depth-resolved images of backscattering or backreflection from biological tissue. In the brain, imaging depths of up to and exceeding 1 mm are possible with OCT. A sample OCT intensity image of the brain through a cranial window (Fig. 1A) is shown in Fig. 1B. Preliminary studies of brain activation with OCT intensity images suggesting laminar activation have previously been performed (Maheswari et al., 2003; Chen et al., 2008). While OCT intensity images enable an unprecedented combination of penetration depth and resolution, the imaging technique is hampered by a lack of specificity. In particular, scattering from different cells are indistinguishable unless further image processing techniques are applied.

A number of OCT methods have since been developed for the visualization of blood vessels within scattering tissue (Fingler et al., 2007; Mariampillai et al., 2008; Tao et al., 2008; Vakoc et al., 2009; Wang et al., 2007). These methods all share the feature that motion is used as a contrast mechanism. Recently, a highly sensitive method was proposed to separate both dynamic (Fig. 1C) and static (Fig. 1D) signals in cortical tissue (Radhakrishnan and Srinivasan, 2013). Maps of dynamic scattering, or “angiograms,” can be considered as perfusion maps, where the source of contrast arises from a combination of motion and scattering. Previously, using the OCT angiography technique, imaging of changes in dynamic red blood cell (RBC) content during functional hyperemia accompanying neuronal activation was demonstrated (Radhakrishnan and Srinivasan, 2013). Here, depth-resolved changes

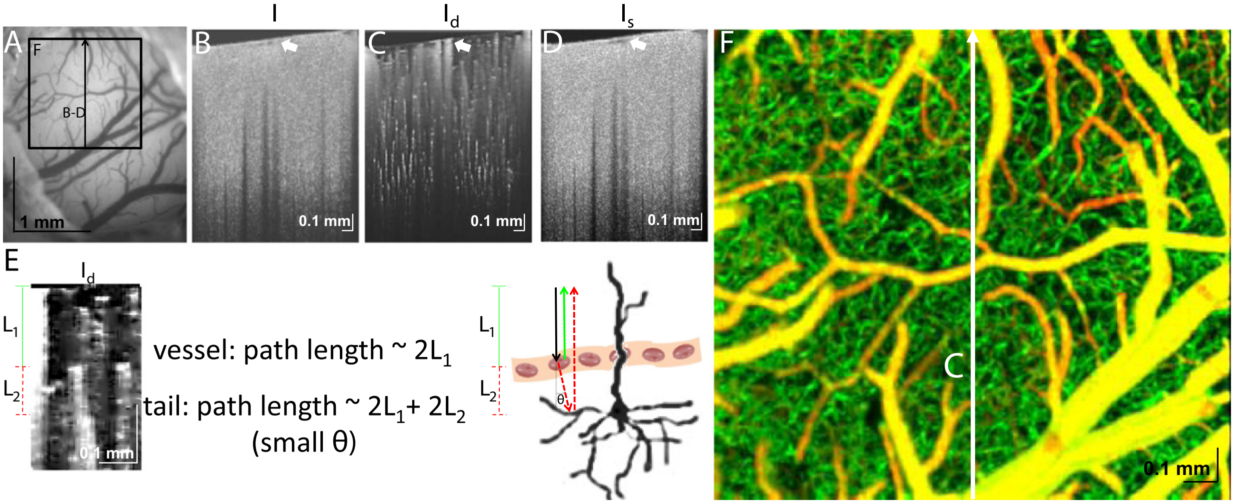

Fig. 1. OCT angiography increases specificity for dynamic scattering from moving blood cells. (A) A photograph of the craniotomy under green light, showing the location of repeated OCT scans. (B) Conventional OCT intensity image includes all scattering from brain tissue, including the extravascular space. A complex filtering method was used to isolate dynamic signal intensity (C) and static signal intensity (D), as described in the Appendix A. The enhancement of a vascular region in (C) and the suppression of a vascular region in (D) relative to (B) are highlighted by a white arrow. (E) Physical model for multiple scattering tails in dynamic signal intensity includes extravascular backscattering and RBC forward scattering. (F) Color-coded angiogram, with superficial vasculature colored orange/yellow and deep vasculature colored green.

in RBC content and speed are imaged to comprehensively investigate the microvascular response to neuronal activation.

Optical Coherence Tomography (OCT) system setup

A 1310 nm spectral/Fourier domain OCT microscope (Leitgeb et al., 2003), shown in Supplementary Fig. 1A, was constructed for in vivo imaging of the rat cerebral cortex. The light source consisted of two superluminescent diodes combined using a 50/50 fiber coupler to yield a bandwidth of 150 nm. The axial (depth) resolution, defined as the point spread function measured from a mirror, was 4.8 μm in air (3.6 μm in tissue). A spectrometer with a 1024 pixel InGaAs line scan camera operated at 47 kHz. Imaging was performed with a 5× objective, yielding a transverse resolution of 7.2 μm. The system sensitivity was measured to be approximately 100 dB.

Optical Coherence Microscopy (OCM) system setup

Optical Coherence Microscopy (OCM) is similar to OCT, with the exception that tighter focusing is achieved and the axial confocal gate is comparable in size to the coherence gate (Izatt et al., 1994). A 40× objective was used for in vivo imaging of cytoarchitecture, as previously described, using OCM (Srinivasan et al., 2012a). The cortical layers were determined directly based on cytoarchitecture (minimum intensity projection) from in vivo imaging.

Animal preparation

The animal procedures were approved by the Institutional Animal Care and Use Committee at UC Davis. Male Sprague-Dawley rats ($n = 9$; 250–350 g) were used in this study. The rats were initially anesthetized with 2–2.5% v/v isoflurane with a gas mixture of 80% air and 20% oxygen and tracheostomy for mechanical ventilation and cannulation of the femoral artery for blood pressure monitoring and vein for anesthetic administration were performed. Following catheterization, the animal was mounted on a stereotactic frame and a craniotomy was performed. Briefly, the scalp was retracted and a metal plate was attached to the exposed skull using bone screws. Using a dental burr, a ~5 × 5 mm^2 region over the left forepaw region was thinned to translucency and was removed along with the dura. The exposed cortex was filled with 1.5% agarose (Sigma Aldrich, MO USA), mixed in a CSF (pH 7.4; KCl 5 mM, NaCl 125 mM, Glucose 10 mM, $CaCl_2$ 3 mM, and $MgCl_2$ 1 mM, Sigma Aldrich, MO USA), and covered with a glass coverslip. Dental acrylic was used to seal the cranial window to the skull. To relieve excess intra-cerebral pressure, a ventriculostomy of the IVth ventricle was performed.

Following the surgical procedures, the anesthesia was changed to alpha-chloralose (loading dose — 40 mg/kg; maintaining dose — 40–50 mg/kg/h). Throughout the surgical and imaging procedures, the blood pressure was monitored (SYS-BP1, WPI Inc., USA) via a transducer (BLPR2, WPI Inc., USA) connected to the arterial cannula and the animal's core temperature was maintained at 37° Celsius using a heating blanket (Harvard Apparatus USA). Periodic measurement of blood gases and pressure were performed to ensure values were within physiological ranges (pH: 7.39 ± 0.03, Pa_{CO2}: 35.5 ± 3.1 mm Hg, Pa_{O2}: 149 ± 14 mm Hg, MABP: 103 ± 18 mm Hg).

Angiography protocol

The activated area was first determined coarsely with a ball electrode, and then more precisely from an image of the hemodynamic response from OISI reflectance imaging at 570 nm. A two-dimensional angiography protocol was used to investigate depth-resolved changes with high spatiotemporal resolution. Repeated B-scans over 1.5 mm (transverse) × 1.54 mm in (depth) were performed, with approximately 7 ms per frame (B-scan). Scanning was asynchronous with stimulus presentation. Therefore, the stimulus waveform and frame (B-scan) triggers were recorded by a separate data acquisition card (in PC2 in Supplementary Fig. 1A) to determine the precise location of stimuli relative to the acquired OCT frames. The focus was placed approximately in cortical layer IV, and regions with large pial vasculature were avoided. As an additional control, in several animals the focus was placed at the surface and similar trends in the laminar response magnitudes were obtained (Supplementary Fig. 2). Thus, the responses were representative of the microvasculature. A representative angiogram of the microvasculature with the location of the OCT scan is shown in Fig. 1F (surface vessels colored yellow/orange, deep vessels colored green).

OCT metrics

RBCs impact OCT signals in two distinct and quantifiable ways; through backscattering and attenuation versus depth. Therefore, two complementary metrics were used to assess microvascular RBC content: 1) *baseline-normalized dynamic backscattering changes* indicate baseline-normalized changes in RBC content, while 2) *attenuation coefficient changes* indicate changes in RBC content, irrespective of baseline values.

Attenuation coefficient

An attenuation coefficient change metric, discussed further in Appendix A, was used to measure changes in red blood cell content. While OCT signal is attenuated by both absorption and scattering with increasing depth, attenuation coefficient changes during activation are likely due to increases in scattering from RBCs in the microvasculature (Radhakrishnan and Srinivasan, 2013). The attenuation coefficient had a similar time course to total hemoglobin (Fig. 2), suggesting a similar physiological origin. In contrast to the dynamic RBC content metric below, the attenuation coefficient does not directly depend on motion of RBCs.

dRBC content

The rationale behind the dynamic RBC content metric (Radhakrishnan and Srinivasan, 2013; Srinivasan et al., 2012b) is briefly described here and discussed in detail in Appendix A. The measurement principles are analogous to those employed by laser Doppler Flowmetry (LDF), with the exception that much smaller volumes (determined by the OCT axial and transverse resolutions) are analyzed. In LDF the total power of the Doppler shifted signal is assumed to be proportional to the concentration of moving blood cells in tissue (Fabricius et al., 1997). Similarly, the total power in the OCT dynamic signal in a voxel is assumed to be proportional to time-averaged red blood cell content. Just as the LDF signal is typically normalized to the mean photocurrent to achieve a measure that does not depend on tissue reflectivity, the dynamic signal is normalized to the signal from nearby static tissue to achieve depth-specific backscattering measurements that are insensitive to variations in attenuation (Radhakrishnan and Srinivasan, 2013). Our experimental results in flow phantoms confirmed that backscattering is linear in red blood cell content up to a hematocrit of 45% across a range of flow rates (Supplementary Fig. 3C).

dRBC speed

Analogous to LDF, the spectral bandwidth of the fluctuations in the complex OCT signal is related to RBC speed (Ren et al., 2012). Therefore, the bandwidth of the dynamic component of the power spectral density was taken as a measure of dRBC speed (Srinivasan et al., 2012b). This metric is discussed further in Appendix A and Supplementary Fig. 6. Our experimental results showed that the dRBC speed metric might increase with hematocrit at higher hematocrit due to multiple or cooperative scattering effects (Supplementary Fig. 3E). Therefore, we explicitly drew conclusions based only on the kinetics and not magnitudes of dRBC speed changes.

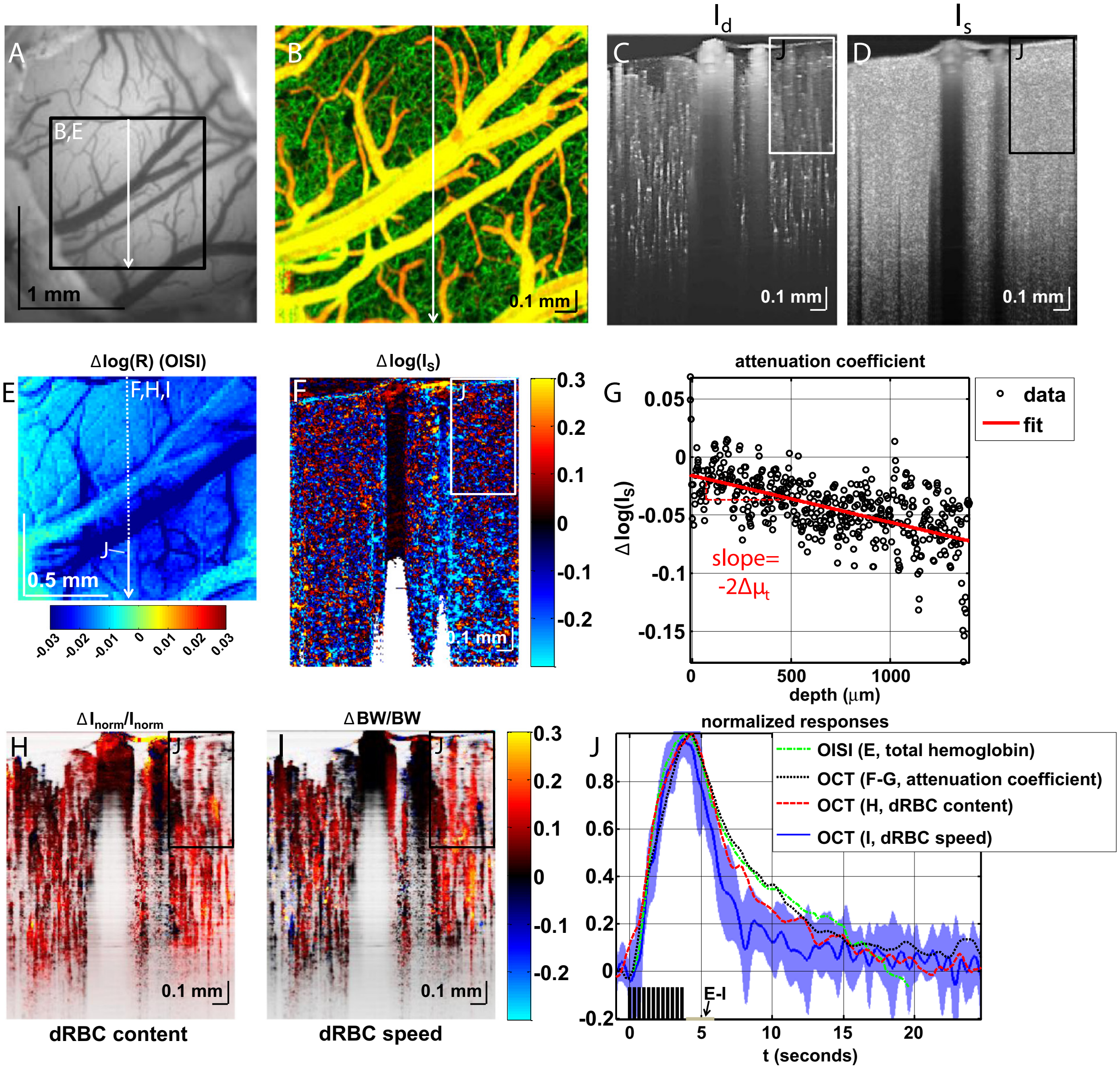

Fig. 2. OCT performs imaging of dRBC content and speed. Photograph of rat somatosensory cortex with angiogram showing surface vessels colored in yellow/orange and deep vessels colored in green. A single OCT scan is shown as a white line across the angiogram. (C–D) Dynamic intensity image (I_d), which shows dynamic signal from blood cell components, and static scattering image (I_s), which shows signal from other tissue. (E) OISI peak activation map (4–6 s post-stimulus onset) of logarithmic reflectance changes at an isobestic wavelength of 570 nm, proportional to changes in total hemoglobin with a negative constant of proportionality. OCT metrics of attenuation coefficient (F–G), dRBC content (H), and dRBC speed (I, mean of 16 vessels +/− s.d.) are shown (see Appendix A and Supplementary Fig. 6 for further description of metrics) at peak activation. (J) When metrics are determined from comparable cortical regions, differing kinetics imply different hemodynamic underpinnings. Particularly, the attenuation coefficient and dRBC content agree with OISI reflectance changes (averaged over solid line in E), whereas dRBC speed returns to baseline more promptly after stimulus cessation. Based on the well-accepted correspondence of reflectance at an isosbestic wavelength and hemoglobin content, we conclude that the dRBC content metric closely tracks changes in hemoglobin via RBC backscattering, and is minimally sensitive to speed.

Stimulus protocols

Two hypodermic needles were inserted into the plantar surface of the rat forepaw. The needles were connected by alligator clips to a stimulus isolator that delivered 200 μs pulses just below motor threshold (~1.5 mA) when receiving computer controlled triggers at either i) 3 Hz for 4 s (block paradigm), or ii) 1–5 Hz for 4 s (event-related paradigm).

Block

In the block design, electrical pulses were delivered for 4 s at 3 Hz with an interstimulus interval of 21 s (block period of 25 s). 12 blocks were presented per run, with approximately 5 min between runs.

Event-related

In the event-related design (Dale, 1999), electrical pulses were delivered for 4 s with a varying frequency between 1 and 5 Hz. The mean interstimulus interval for this was about 12 s. Twenty-three stimulus trains were presented per run, with approximately 5 min between runs. In some animals, surface-evoked potential (SEP) responses were recorded with a screw electrode in the skull adjacent to the cranial window over the activated area. The P1 and N1 component (Franceschini et al., 2008) peak voltages and temporal delays were detected automatically in the analysis software.

Optical Intrinsic Signal Imaging (OISI)

The OCT system (Supplementary Fig. 1A) was designed for simultaneous Optical Intrinsic Signal Imaging (OISI) with a CCD camera under green light (570 ± 5 nm). Before OCT imaging, the activated area was coarsely determined with a ball electrode, and then more precisely from an image of the temporal width of the hemodynamic response to a 4 s, 3 Hz stimulus. A dichroic mirror and additional IR blocking filter were used to prevent infrared light from reaching the CCD camera (Supplementary Fig. 1A). As the illumination light for CCD imaging was located at an isosbestic point for oxy- and deoxy-hemoglobin, logarithmic reflectance changes relative to baseline ($\Delta\log(R) = \log(R/R_0) \sim \Delta R/R_0$) at this wavelength are proportional to total hemoglobin changes relative to baseline ($\Delta HbT = HBT - HBT_0$) with a negative constant of proportionality (Sheth et al., 2004). Thus a negative fractional reflectance change relative to baseline corresponds to an increase in hemoglobin relative to baseline. Therefore; simultaneous measurements of logarithmic reflectance changes relative to baseline were used to validate the dRBC content metric as the stimulus frequency was parametrically varied. While RBC content changes are measured based on scattering and ΔHbT is measured based on absorption, agreement of the two signals would strongly suggest a shared hemodynamic underpinning.

Data analysis

The OCT resolution of 3.6 μm in tissue is conventionally defined as the full-width at half maximum of the point spread function. However, in angiograms, the resolution can be degraded by multiple scattering events. In particular, as shown in Fig. 1E, capillaries are accompanied by "tails" of a few hundred microns in axial extent, resulting mainly from red blood cell forward scattering followed or preceded by tissue backscattering (Fig. 1E). These tails may also be caused by changes in path length as high refractive index red blood cells cross the beam path. The dynamic scattering tails tend to diminish as path length increases due to attenuation by scattering. Pial arteries and veins, due to their large sizes and high hematocrits, generally have longer multiple scattering tails that obscure the visualization of underlying microvessels. As multiply scattered photons always have a larger path delay than singly scattered photons, vessels are only blurred in the direction of positive path lengths; hence, it is still possible to localize vessels accurately in depth by the superficial backscattering. We performed axial averaging over 150 μm, approximately the range defined by the multiple scattering tails when determining laminar response characteristics shown below. Responses for both stimulation protocols were determined using a linear time-invariant prediction model (Dale, 1999), including a slow 4th order polynomial term to account for baseline fluctuations.

Laminar profiles of the average fractional change, peak fractional change, undershoot ratio, time to peak, time to half peak, onset time, and return time were plotted (mean ± s.e.m.). The average and peak fractional changes were determined based on the entire post-stimulus time interval. In addition to comparison of laminar profiles, response magnitudes and times were partitioned according to cortical layer. As each run had a different response magnitude, the response magnitude was divided by the maximum response magnitude at depths greater than 200 μm for each run. As each run had different response kinetics, the minimum time at depths greater than 200 μm was subtracted from the laminar temporal profile for each run. Cortical layers were identified by in vivo imaging of cytoarchitecture using OCM, and are in agreement with previous studies (Masamoto et al., 2004).

Results

In order to establish the interpretation of OCT metrics (attenuation coefficient, dRBC content, dRBC speed), simultaneous OISI imaging was performed (Fig. 2) and time courses were compared during parametric variation of stimulus frequency (Fig. 3). Fig. 2A shows a grayscale image of the rat brain through a cranial window under green light (570 nm) illumination, along with an OCT angiogram (maximum intensity projection based on dynamic scattering) over a region of interest (Fig. 2B). The total dynamic signal intensity and static signal intensity images are shown in Figs. 2C–D. An OISI map of the logarithmic reflectance change at peak activation relative to baseline is shown (Fig. 2E). The difference in the logarithmic OCT static signal intensity at peak activation relative to baseline is shown (Fig. 2F). Decreases in signal were more pronounced in deeper cortical layers, suggesting that the attenuation coefficient increases during activation. Thus, a change in the attenuation coefficient, $\Delta\mu_t$, could be determined by fitting the axial static signal profile versus depth (Fig. 2G, Appendix A). A dRBC content metric, $\Delta I_{norm}/I_{norm}$, and a speed metric, ΔBW/BW, are also shown (Figs. 2H–I). When metrics were determined over a region of 500 μm corresponding approximately to the OISI penetration depth (rectangles in Figs. 2C–D,F,H, and I), normalized time courses showed that the OCT attenuation coefficient and dRBC content kinetics agreed with those of total hemoglobin (Fig. 2J).

Fig. 3A shows kinetics of logarithmic reflectance changes at an isosbestic wavelength measured by OISI, compared to the three OCT metrics (Figs. 3B–D). The peak fractional change in total hemoglobin was estimated to be 12–24%, which agrees with the ~19% peak fractional change in RBC content (Fig. 3C). In order to convert OISI logarithmic reflectance changes to fractional changes in total hemoglobin, a baseline HbT concentration of 100 μM (Kohl et al., 2000) and a path length of 0.5–1 mm (Dunn et al., 2005; Mayhew et al., 2000) were assumed. Additionally, OISI total hemoglobin time courses were similar to OCT attenuation coefficient and dRBC content (Figs. 3E–F) and dissimilar to dRBC speed (Fig. 3G). This result was confirmed by statistical comparison of R^2 values (Fig. 3H). This result is also supported in our ex vivo studies that demonstrated a linear relationship between hematocrit and backscattering (Supplementary Fig. 3C). Taken together, these data suggest that the dRBC content metric can be viewed as, in essence, a depth-resolved measure of HbT changes.

Fig. 4 shows imaging of the laminar dRBC response to functional activation. The angiogram (Fig. 4A) showing the scan location along with dynamic and static signal intensity (Figs. 4B–C) images are shown. The dRBC content is plotted as a time course (Fig. 4D), along with predictions of response and baseline fluctuations (polynomial) from a linear time-invariant model (Dale, 1999). Single trials show high repeatability (Fig. 4E). Based on 12 single trials, temporal characteristics were calculated as shown in Fig. 4F based on normalized time courses. The onset time, in particular, was defined as the time required for the response to ascend past a level of twice the noise standard deviation at the same depth. The average fractional change, peak fractional change, time to half peak, and time to half peak are shown in Figs. 4G–K (mean ± s.e.m.), demonstrating laminar trends. Both the time to half peak (Fig. 4I), time to half peak (Fig. 4J), and onset time (Fig. 4K) show a minimum around 500–600 μm, while the average fractional change (Fig. 4G) shows a peak around 800 μm.

Fig. 5 shows analysis of laminar profiles across animals. For this analysis, RBC content responses based on a linear time-invariant prediction model (Fig. 4D) across an entire run were used. Clear amplitude differences were observed between layers, with the peak in the middle cortical layers (Fig. 5A). Laminar differences in kinetics were observed as well (Figs. 5B–D). Clear differences in fractional changes (Figs. 5E–F) and timings (Figs. 5G–I) were visualized, with the general trends agreeing with the single subject in Fig. 4. When averaging was performed over all runs and all animals, the peak fractional changes showed a maximum at 654 ± 114 μm depth (mean ± std. dev.), while the average fractional changes showed a maximum at 647 ± 156 μm depth (mean ± std. dev.). When data were grouped according cortical layers based on in vivo OCM imaging of cytoarchitecture as shown in Fig. 6A, layers IV and V showed the largest (Figs. 6B–C) and earliest (Figs. 6D–F) responses. Intra-animal normalization was performed prior to hypothesis testing by dividing by the maximum across all depths greater than 200 μm (for magnitudes in Figs. 6B–C), or subtracting the minimum across all depths greater than 200 μm (for times in Figs. 6D–F). In

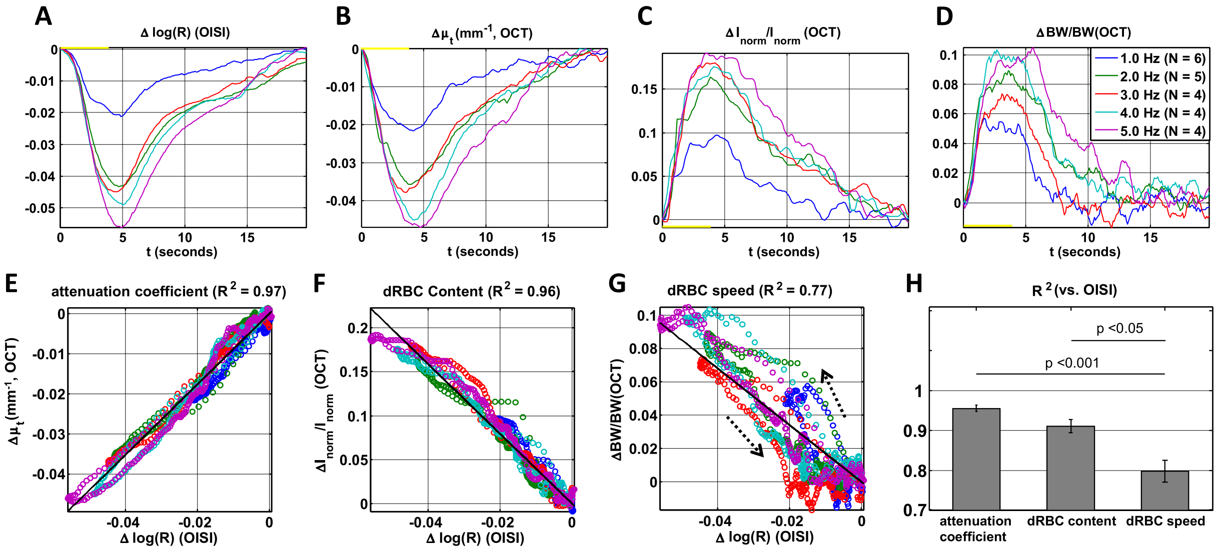

Fig. 3. Hemoglobin kinetics match OCT attenuation coefficient and dRBC content, but not dRBC speed. Deconvolved OISI (A, 570 nm) and OCT responses (B–D) to event-related stimulus paradigm with 1–5 Hz frequencies. (E–G) Parametric plots of OCT metrics (averaged over the first 500 μm, corresponding to the OISI depth) versus OISI reflectance for the data in A–D. OCT responses were convolved with a sliding window corresponding to the CCD integration time (~1 s). OCT attenuation coefficient and dRBC content time courses closely match those of hemoglobin absorption (E–F). By contrast, the OCT dynamic signal bandwidth, theoretically related to speed, exhibits significantly faster kinetics than hemoglobin absorption (G, dotted arrows show progression of time), particularly in the return to baseline and undershoot. A least squares linear fit to the data in E–G is shown in black. (H) R^2 values, determined from parametric plots (N = 4, mean +/− s.e.m.), are higher for the attenuation coefficient and dRBC content metrics, suggesting that these metrics are biophysically linked more closely to hemoglobin content than dRBC speed. To determine p-values, ANOVA was performed on the z-scores obtained by Fisher transformation followed by Tukey's honestly significant difference test.

agreement with these results, the attenuation coefficient increase, due to an increase in red blood cell number per unit cortical volume during activation, was larger in layer IV than in the other cortical layers (Supplementary Fig. 4).

Neurovascular coupling analysis was performed to assess the relationship of layer-specific hemodynamic changes to both cortico-cortical synaptic activity (N1) and thalamocortical inputs (P1). Measured electrophysiological responses (Supplementary Fig. 5A) occurred within tens of milliseconds after the first stimulus pulse, while hemodynamic responses were delayed (Supplementary Fig. 5B). A linear model was applied with each of the three predictors (P1, N1, and stimulus) as independent variables, using the model R^2 as a criterion for comparison (Supplementary Fig. 5C). The impulse response derived from the predictor (N1 peak) with the highest R^2 is shown (Supplementary Fig. 5D). Comparison across layers shows that the coefficients of determination between N1 and dRBC content changes were significantly higher in the middle cortical layers than the coefficients of determination between P1 and dRBC content changes (Supplementary Fig. 5E). Thus, while the earliest and largest hemodynamic responses coincided spatially with majority of thalamocortical synapses in the middle cortical layers, ensuing cortico-cortical synaptic activity better predicted these responses.

Fig. 7 shows laminar trends in the undershoot ratio, defined as the area of the negative response lobe to the area of the positive response lobe. If undershoots were observed in HbT (as determined by OISI, typically in surround regions), undershoots in RBC content (as measured by OCT angiography) were also observed. Figs. 7A–B shows OCT and OISI responses with increasing undershoot ratios further from the center of activation (Chen et al., 2011). OCT angiography (Figs. 7C–D), when performed regions with OISI undershoots, also exhibited undershoot, with the highest relative undershoot ratio near the cortical surface (Fig. 7E). When laminar responses were investigated in runs located where OISI exhibited undershoots (Figs. 7F–G), the undershoot ratio was found to be the largest at the cortical surface and the smallest in the middle cortical layers. Normalization was performed by dividing by the maximum across all depths greater than 200 μm before hypothesis testing, since the degree of undershoot varied across runs and animals.

While the response magnitudes and relative undershoots varied across cortical layers, a mismatch between dRBC content and dRBC speed persisted across layers (Fig. 8). The return time (Fig. 8A) was consistently longer across cortical layers for dRBC content compared to dRBC speed (Figs. 8B–C). Correspondingly, the temporal mismatch between dRBC content and speed, determined based on normalized time courses as shown in Fig. 8D, was positive across layers (Fig. 8E). No statistically significant differences were detected between layers.

Discussion

Analysis of laminar hemodynamics represents one avenue to elucidate neurovascular coupling mechanisms, since cellular and vascular architecture (Blinder et al., 2013), as well as neuronal activity and metabolism (Herman et al., 2013), vary across the cortical column. In this study, we applied novel OCT metrics based on RBC scattering for the study of laminar hemodynamic changes combined with OCM to image cytoarchitecture and delineate cortical laminae. Time courses and magnitudes of depth-averaged RBC content changes measured by OCT were correlated with simultaneous changes in HbT concentration measured by conventional OISI (Fig. 3), supporting further use of the OCT metrics to quantitatively assess amplitudes and kinetics. The layer-resolved OCT measurements enabled by our methods led to a number of novel findings.

The RBC response is largest in the middle cortical layers

Our results show the largest RBC responses occur around the border of layers IV and V (Figs. 5E–F). The closest analogs of our dRBC content metric in the literature are RBC linear density changes measured by two-photon microscopy and hemoglobin changes measured by OISI (Fig. 3). Relative changes in red blood cell linear density during activation measured by two photon microscopy near the cortical surface are typically found to be much smaller than speed changes, and are altogether absent in some studies (Kleinfeld et al., 1998; Stefanovic et al., 2008). On the other hand, other lines of evidence apparently contradict this data. First, laminar optical tomography (LOT) (Hillman et al., 2007)

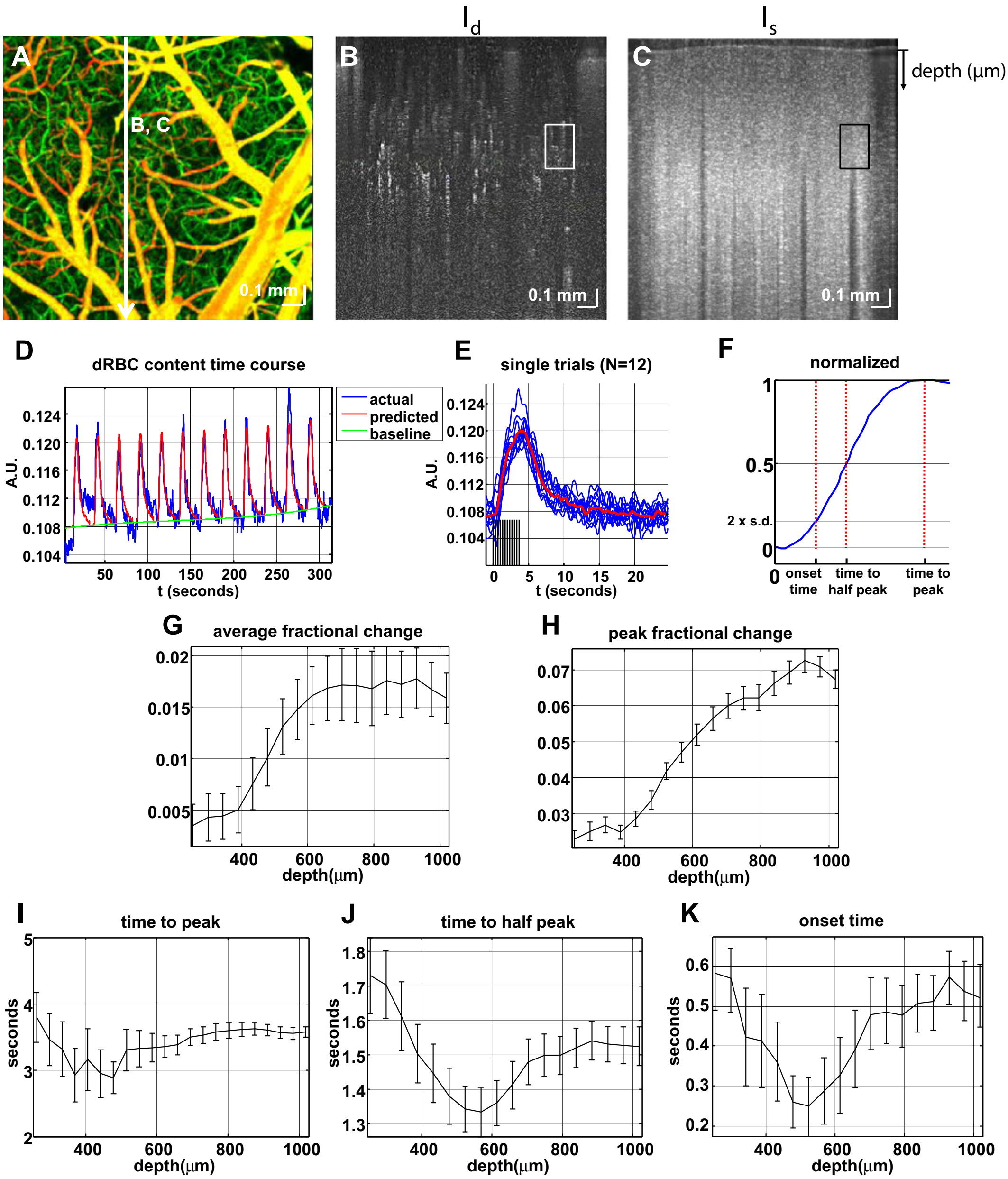

Fig. 4. Single trial imaging of laminar dRBC response characteristics in an individual subject. (A) OCT angiogram with scan location as a line. Dynamic (B) and static (C) signal intensity images. (D) Normalized OCT intensity shows a response to individual stimuli (3 Hz, 4 s) over the boxed region of interest shown in B–C. (E) OCT responses to individual stimulus trains are observable. (F) Calculation of onset time, time to half peak, and time to peak from normalized response. (G–K) Average fractional change, peak fractional change, time to peak, time to half peak, and onset time, plotted as mean ± s.e.m across 12 trials.

shows significant hemoglobin changes in capillaries in the middle cortical layers. Second, parenchymal, presumably capillary-level, hemoglobin changes are routinely measured by OISI (Malonek et al., 1997; Nemoto et al., 2004; Vanzetta et al., 2005). Third, mapping based on hemoglobin absorption yields identical results to mapping based on fluorescence of an intravascular dye (Frostig et al., 1990), suggesting but not proving that the plasma and hemoglobin increases are co-localized and functionally specific. Fourth, RBC and plasma volume have similar transients during activation (Herman et al., 2009). Fifth, large microvascular plasma volume changes are observed in middle cortical layers by functional MRI (Harel et al., 2006; Lu et al., 2004; Mandeville and Marota, 1999; Smirnakis et al., 2007; Zhao et al., 2006). Thus, the absence of linear red blood cell density increases in two-photon microscopy studies performed near the cortical surface seems to challenge the more macroscopic imaging results.

By investigating changes over a mesoscopic scale, our study helps to bridge the gap between these disparate results. We showed that RBC changes are small with prominent undershoots in surface microvasculature where two-photon measurements are typically made but much larger with less prominent undershoots in deeper cortical layers probed by laminar optical tomography and fMRI (Fig. 7G). Our results complement prior fMRI findings by strongly implying that red blood cell volume increases along with blood plasma volume in the middle cortical layers. Increases in capillary RBC linear density have been assumed to accompany capillary dilation (and hence, microvascular cerebral blood volume increases) via increased stacking density (Chaigneau et al., 2003). Taken together, these results strongly suggest microvascular dilation in deeper cortical layers.

While the large RBC changes in the middle layers (Figs. 6B–C) parallels previous fMRI studies that measured plasma volume, a recent two-

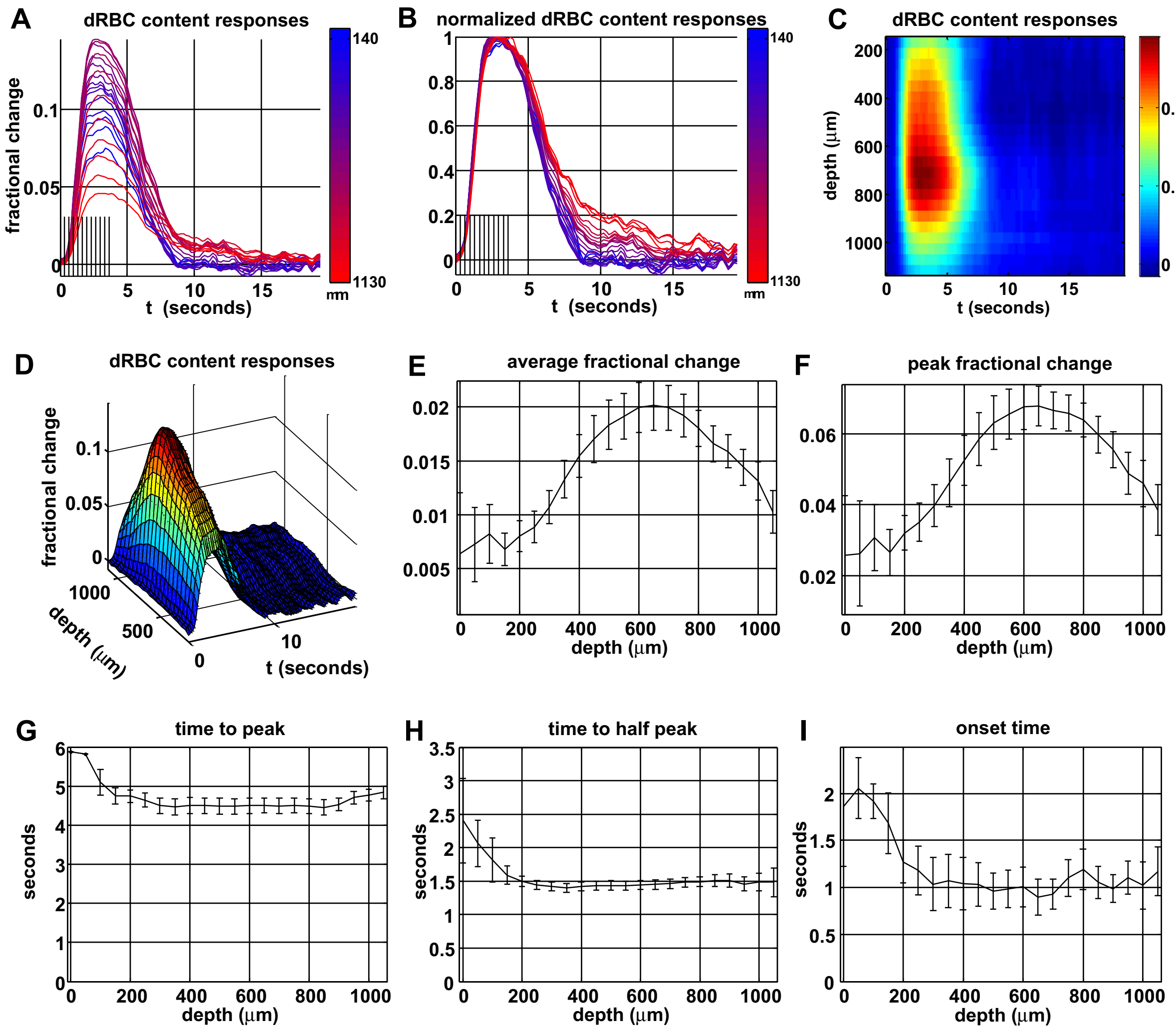

Fig. 5. Trends in laminar dRBC response characteristics across animals. Responses were obtained from a run of 12 trials (3 Hz, 4 second stimuli, 21 second ISI). Un-normalized (A) and normalized (B) responses from a single animal, with depth color-coded from blue (more superficial) to red (more deep). Responses are shown in false color vs. depth and time (C), and as a surface plot (D). (E–I) Laminar profiles for average fractional change, peak fractional change, time to peak, and time to half peak, and onset time, pooled over all animals (N = 15, mean +/− s.e.m.), are shown. Timing for dRBC speed was not explicitly investigated due to lower signal-to-noise ratios.

photon microscopy study (Tian et al., 2010) showed comparable arteriole dilation magnitudes at all depths. Indeed as deeper capillary beds are served by longer diving arteriolar segments, deeper capillary beds would see a larger drop in total network resistance than superficial layers served by shorter arteriolar segments, even if relative arteriole diameter changes are depth-invariant. Moreover, the probability density of primary arteriole branches shows a maximum in layer IV (Blinder et al., 2013). Thus, depth-invariant relative arteriolar dilation (Tian et al., 2010) may indeed be consistent with depth-dependent RBC responses seen in this study.

Early and prominent hemodynamic changes in layer IV may explain laminar BOLD

Our results highlight an early and prominent increase in RBC content in the middle cortical layers (Fig. 6), which, taken together with the large plasma volume changes in these layers (Shih et al., 2013), suggest early and prominent blood volume changes. The large RBC speed changes observed in these layers (data not shown) furthermore imply that flux changes are also the largest in layer IV. Therefore, our purely hemodynamic data potentially explain laminar variations in BOLD onset time (Yu et al., 2014). The BOLD signal mainly depends on deoxyhemoglobin, but has a weaker dependence on blood volume (Obata et al., 2004). Thus, an early and prominent flux or volume change in microvasculature (arterioles and capillaries) in the middle cortical layers (Yu et al., 2012), occurring before the filling time and transit time required for oxygenated blood to reach the veins, may explain the early BOLD response that is routinely observed in these layers.

While our methodologies were (by design) insensitive to oxygenation, metabolic differences in cortical layers may accompany differences in hemodynamic response magnitudes. Histological studies also have shown that layer IV has a relatively high metabolism (Chmielowska et al., 1986; Wong-Riley, 1989). Thus, without depth-resolved metabolic information we cannot directly predict BOLD fMRI from our data. Laminar investigation of metabolism will be a subject of future studies.

Negative RBC responses are most prominent superficially

In the post-stimulus period, negative microvascular RBC responses comprising the “undershoot” were most prominent superficially and diminished in deeper cortical layers (Fig. 7). This depth-resolved data complements prior optical studies that examined undershoots in the center versus the surround (Chen et al., 2011). A rapid superficial return to baseline of cerebral blood volume (CBV) coupled with a persistent deep CBV elevation has been used to explain laminar differences in the BOLD undershoot (Yacoub et al., 2006; Zhao et al., 2007). Recently

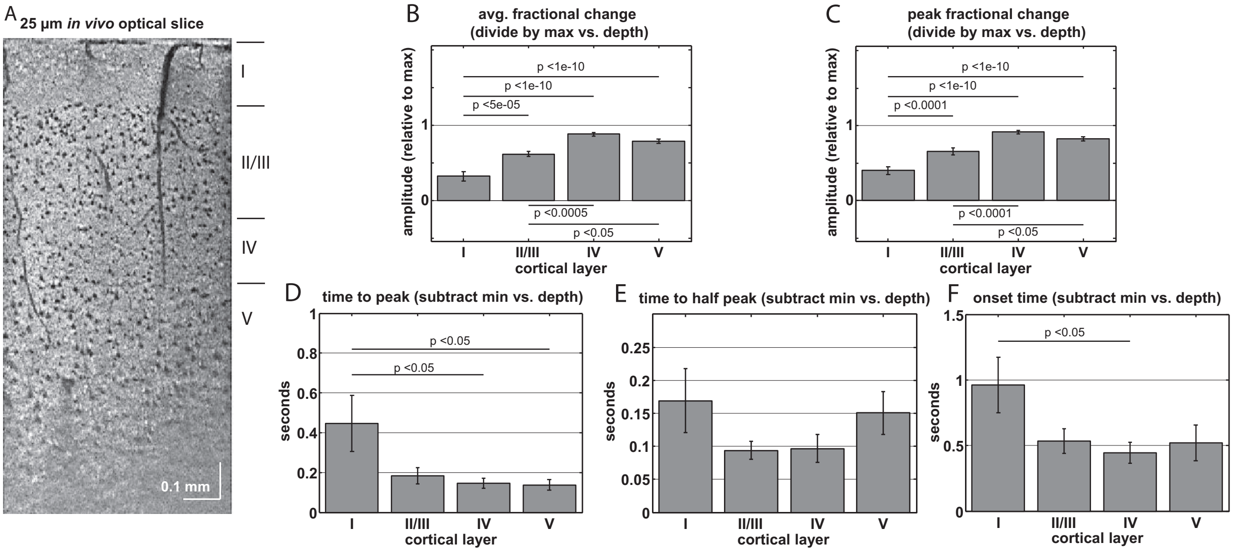

Fig. 6. (A) Based on in vivo OCM imaging of cytoarchitecture, cortical layer depth ranges were defined and laminar data were grouped accordingly. Normalized time-averaged and peak fractional changes (B–C, after division by max vs. depth) and time to peak, time to half peak, and onset time (D–F, after subtraction of min vs. depth), are shown as bar plots (N = 15, mean +/− s.e.m.), showing that the largest and earliest hemodynamic responses occur in middle cortical layers. Before averaging across runs and animals, the minimum time across depths greater than 200 µm was subtracted from each individual time profile. The p-values were calculated by one-way ANOVA followed by Tukey's honestly significant difference test for comparisons between layers, and only comparisons with $p < 0.05$ are shown. Speed showed very similar laminar trends to dRBC content (data not shown).

superficial reductions in blood flow coupled with deeper increases in blood volume were co-localized with regions exhibiting negative BOLD (Goense et al., 2012), a closely related phenomenon. Here, we show more directly, that RBC content returns to baseline rapidly superficially and persists in the middle cortical layers after the stimulus ends. Finally, our finding of a larger constriction ratio superficially agrees qualitatively with the higher fractions of GABA inhibitory neurons in the upper cortical segment (Winfield et al., 1980) and the purported role of interneurons in vasoconstriction (Cauli et al., 2004).

A “flow-volume mismatch” persists across cortical layers

Our data show that RBC speed returns to baseline earlier than RBC content across cortical layers. While the RBC speed response is rapid on both stimulus onset and offset, the RBC content response is considerably slower than RBC speed on stimulus offset. The fact that microvascular RBC volume remains high after a stimulus, taken together with the fact that microvascular plasma volume similarly persists (Mandeville et al., 1999), implies that the total microvascular volume remains elevated after the stimulus. Whether the persistent microvascular volume increase after flow and arterial diameter have returned to baseline is the result of active capillary dilation remains to be seen. Nevertheless, these results strongly argue for a flow-volume mismatch in the microvasculature and provide one possible mechanism for a BOLD undershoot. However, oxygenation was not measured in these studies, and RBC content in pial veins was not directly examined; hence we cannot exclude other mechanisms for the BOLD undershoot.

In our validation studies, the speed metric may increase with hematocrit at high hematocrits, likely due to cooperative or multiple scattering effects (Supplementary Fig. 3E). However, even if this hematocrit dependence had made our metric sensitive to flux (the product of speed and linear density) at high hematocrits, our conclusions regarding the “flow-volume mismatch” would remain unchanged.

Neural correlates of the hemodynamic response

This study shows that the earliest, largest, and most sustained RBC increases coincide with the locus of cortical inputs (layer IV) and outputs (layer V). Based on these findings, it may be tempting to assign neural correlates to the hemodynamic response based on the known functions of cortical layers IV and V. However, our results do not necessarily imply that either the thalamocortical synaptic activity or the output spiking activity “drive” or cause the hemodynamic response. On the contrary, as a relatively small number of synapses (even in the input cortical layers) are thalamocortical, (Logothetis, 2008), even the vascular response in layer IV may occur via cortico-cortical synaptic activity. This is supported by our finding of tighter coupling between RBC content and the N1 SEP component than the P1 SEP component, even in layers IV–V (Supplementary Fig. 5E).

Our data also directly confirm the previous suggestion that hemodynamic changes occur earliest in the middle cortical layers, but evolve over a much longer time scale than could be accounted for by neuronal kinetics (Silva and Koretsky, 2002; Tian et al., 2010). While onset times for dRBC content (Figs. 4K and 5I) are particularly sensitive to motion artifacts, the earliest times to peak (Figs. 4I and 5G) and times to half peak (Figs. 4J and 5H) were observed in the middle cortical layers as well, hundreds of milliseconds earlier than the cortical surface. The response to the first electrical pulse shows that the latency between P1 and N1 is 10–20 ms (Supplementary Fig. 5A). Thus neuronal delays (tens of milliseconds) are an order of magnitude faster than hemodynamic delays (hundreds of milliseconds) from layer IV to the surface. Due to the speed of neural activity propagation across the cortical column (Einevoll et al., 2007), onset times of neuronal activity across layers are unlikely to account for the observed hemodynamic trends. Rather, the hemodynamic response can be affected by i) the release of vasoactive signal from neurons ii) the transmission (diffusion) of signals iii) the uptake of signals by vascular cells, and iv) the action of the vascular cells (Masamoto and Kanno, 2012). Indeed, as layer IV possesses the highest capillary density (Masamoto et al., 2004) and primary arteriole branch density (Blinder et al., 2013), shorter diffusion times and stronger hemodynamic responses are to be expected in this layer.

While RBC quantification is closely linked to the BOLD signal, it is less informative of active neurovascular control than, for instance, arteriolar diameter measured by two-photon microscopy (Tian et al., 2010). Thus, our observations motivate further studies, perhaps with longer and deeper-penetrating wavelengths for nonlinear excitation (Horton et al., 2013; Kobat et al., 2009), that investigate arterial dilation and constriction dynamics before and immediately after a stimulus.

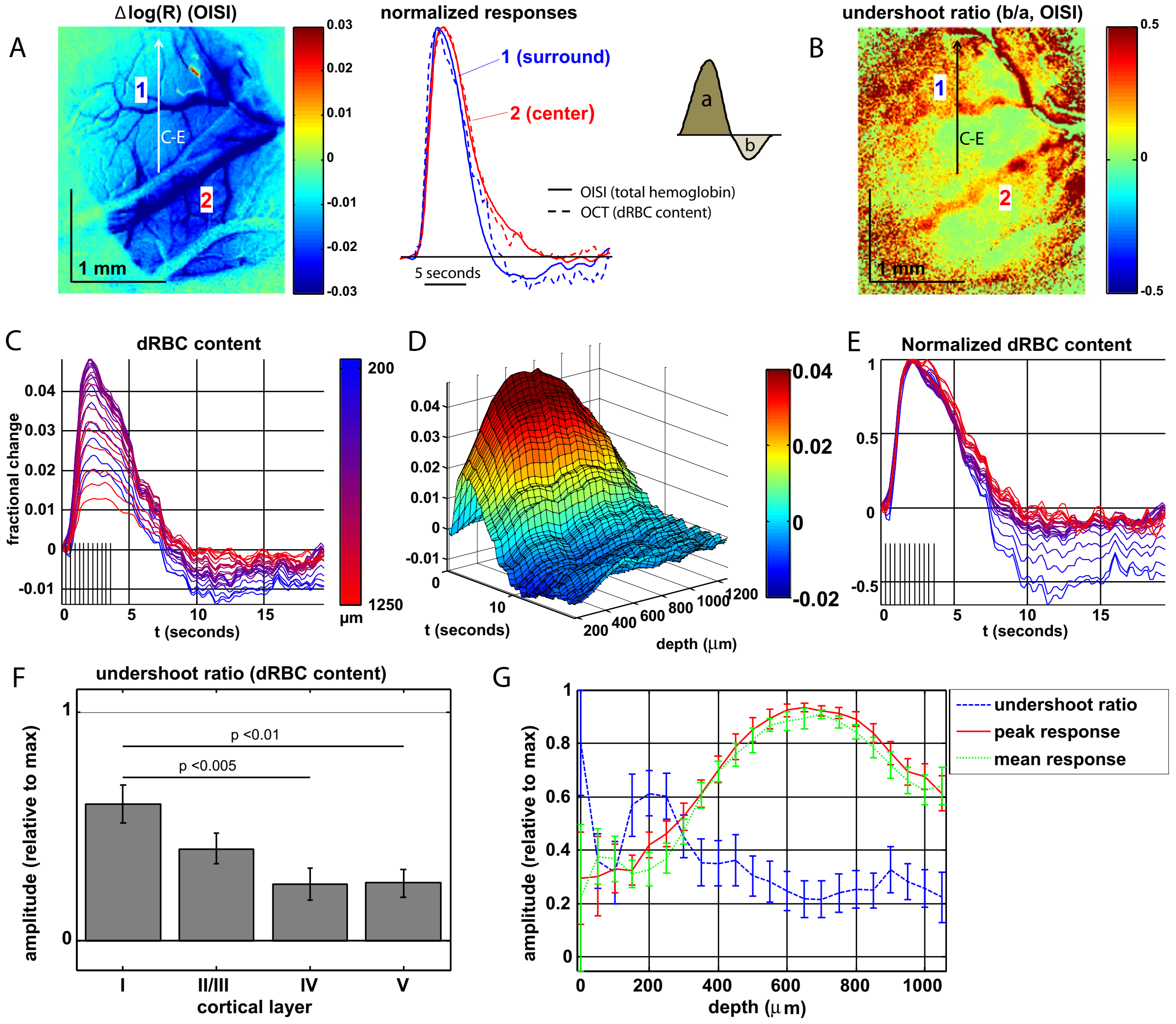

Fig. 7. The undershoot ratio increases near the cortical surface. (A) OISI peak activation map (4–6 s post-stimulus onset) of logarithmic reflectance changes at an isobestic wavelength of 570 nm showing 2 locations with different response characteristics, i.e. different undershoot ratios (inset in A, defined as the area of the negative lobe of the response divided by the area of the positive lobe of the response). OCT dRBC content traces (dashed lines) were determined over a region of 500 μm corresponding approximately to the OISI penetration depth. (B) The undershoot ratio map based on OISI shows that region 1 (surround) return to baseline earlier and undershoots relatively more than region 2 (center). Un-normalized (C–D) and normalized (E) dynamic red blood cell (RBC) content response time courses near region 1, when plotted versus depth, show increased superficial undershoot. When trials across multiple animals that exhibited significant undershoots (>10% at any depth) were investigated, deeper layers were found to have smaller undershoot ratios (F). Comparisons across runs and animals was performed after division by the maximum undershoot ratio at depths greater than 200 μm ($N = 14$). Significance values are calculated by one-way ANOVA followed by Tukey's honestly significant difference test. (G) Whereas the response mean and peak show a maximum in the middle cortical layers, the superficial cortical layers show a larger relative undershoot ratio. Speed undershoot ratios showed similar laminar trends to dRBC content undershoot ratios (data not shown).

Methodological validation

One caveat in the interpretation of our normalized dynamic scattering metric is that systematic RBC orientation changes during hyperemia could potentially affect backscattering, due to anisotropic shape of RBCs. Extensive validation experiments were performed to exclude this possibility. The time courses of RBC content fractional changes agreed with hemoglobin time courses based on the well-accepted technique of intrinsic reflectance imaging (Fig. 3), and RBC fractional change magnitudes agreed with hemoglobin concentration fractional change magnitudes when a reasonable baseline hemoglobin concentration and path length were assumed. Additionally, backscattering was linear in hematocrit across a range of flow rates in an ex vivo blood phantom (Supplementary Fig. 3C). Finally, to avoid confounds of orientation, we deliberately avoided investigation of individual capillary responses, although the data was present, and instead presented data averaged over capillaries of many orientations. We also included the multiple-scattering tails in our analysis in order to obtain a more orientation-independent measure. We also performed depth-resolved fitting of attenuation coefficient changes and found similar laminar trends, strongly suggesting that the RBC number per unit cortical volume indeed increases more in layer IV than other cortical layers during activation (Supplementary Fig. 4C). As with other ubiquitous scattering-based techniques such as laser Doppler, the effects of RBC orientation on scattering in OCT remains an issue that warrants future investigation. Provided that RBC orientation confounds could be mitigated, OCT may prove to be a valuable tool to study RBC changes in pial veins during long stimuli (Drew et al., 2011).

Conclusions

In conclusion, OCT angiography was used to perform laminar imaging of the cortical hemodynamic response to somatosensory activation simultaneously in the superficial and middle cortical layers. The results demonstrate that the earliest and largest increases in RBC content occur in the middle cortical layers, while post-stimulus decreases in RBC content are most prominent superficially. As laminar trends in hemodynamics parallel distributions of excitatory and inhibitory synapses,

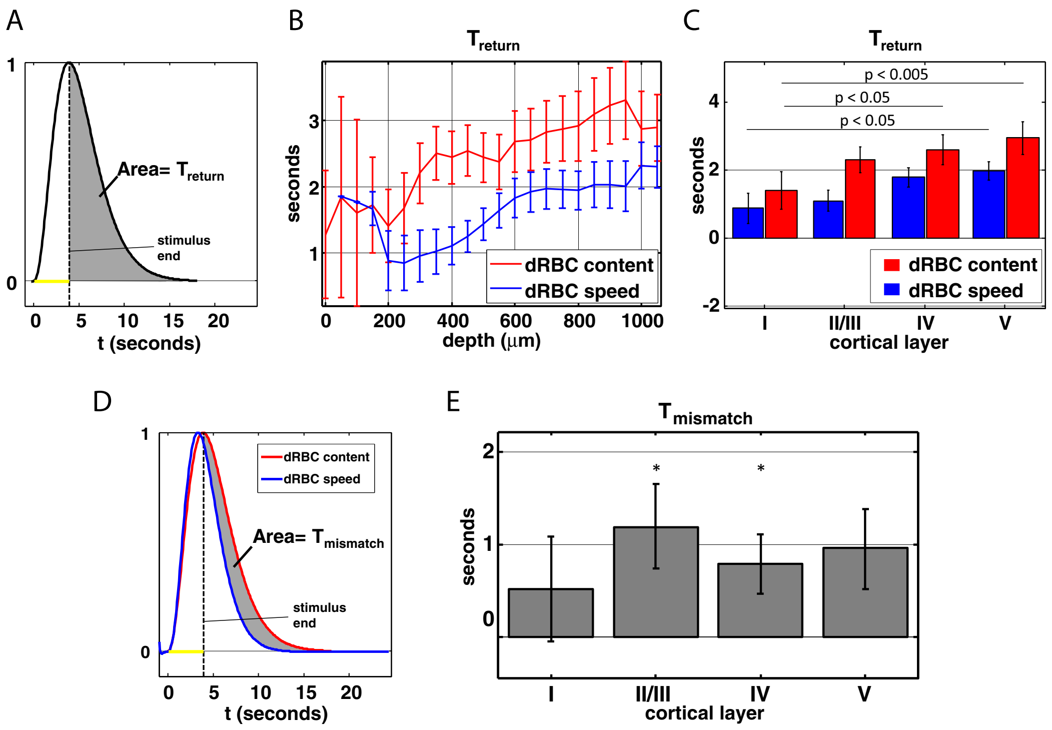

Fig. 8. A robust mismatch between dRBC content and speed across cortical layers was observed. (A) The return time was calculated as the area under the normalized response, starting from the stimulus end. (B) Both dRBC content and speed show increased return times with increasing cortical depth ($N = 7$, mean +/− s.e.m.). The faster superficial return times are in agreement with the larger superficial undershoot ratios (Fig. 7). Critically, dRBC speed consistently returned to baseline *more rapidly* than dRBC content across the cortical depths (B) and cortical layers (C). Significant differences, determined by one-way ANOVA followed by Tukey's honestly significant difference test, after subtraction of the minimum return time at depths greater than 200 μm for each run, are shown. (E) The mismatch time, determined as shown in (D), was found to be greater than zero across cortical layers and was statistically significant in layers II–IV ($N = 7$, $^*p < 0.05$, two-tailed Student's *t*-test).

these results suggest that there are laminar differences in neurovascular coupling. Taken together with fMRI studies that pinpoint layers IV–V as the locus of the most sustained and largest microvascular plasma volume signals, these results also suggest prominent microvascular dilation in the middle cortical layers. Lastly, trends in RBC speed paralleled those in RBC content, with a faster return to baseline that persisted across cortical layers.

Acknowledgments

We acknowledge the support from the National Institutes of Health (R00NS067050), the American Heart Association (11IRG5440002), and the Glaucoma Research Foundation Catalyst for a Cure. We thank Bruce Rosen, Anna Devor, and Maria Angela Franceschini for the general support and advice.

Appendix A

A.1. Dynamic backscattering and red blood cell content

Recently, we developed a quantitative framework to describe scattering constituents of brain tissue (Srinivasan et al., 2012b). This includes both a static scattering component (denoted as I_s), resulting from all neuronal, endothelial, smooth muscle, and glial cell bodies and processes, and dynamic scattering component (denoted as I_d), resulting from scattering and moving blood components. We assume for the purposes of discussion that dynamic scattering from cortical tissue arises predominantly from red blood cells; hence "blood cells" and "red blood cells" will be used interchangeably. The power in the dynamic scattering component is related to red blood cell content, whereas the decorrelation time scale of the dynamic scattering component is related to speed (Srinivasan et al., 2012b). The data processing pipeline is shown schematically in Supplementary Fig. 1B. The complex OCT signal can be divided into static and dynamic and noise components, denoted by subscripts "s" and "d" and "n," respectively.

$$A(x,z,t) = A_s(x,z,t) + A_d(x,z,t) + A_n(x,z,t)$$

The dynamic signal intensity (I_d) can be estimated using a temporal filtering approach as follows:

$$I_d(x,z,T) = \sum_{t=T-\Delta T}^{T+\Delta T} \left|A(x,z,t) * h(t)\right|^2 - \sum_{t=T-\Delta T}^{T+\Delta T} \left|A_{bckgnd}(z,t) * h(t)\right|^2 \cong E\left[\left|A_d(x,z,T)\right|^2\right]$$

The convolution kernel $h(t)$ has frequency response $H(f)$, shown in Supplementary Fig. 7A. Motion correction was performed on all frames prior to convolution. The bias due to noise was corrected by applying an identical filter to a background region of the image and subtracting the result, as shown above. The filter characteristics were chosen to ensure that I_d was insensitive to speed changes and closely approximated the scattering from moving red blood cells. Higher cutoff frequencies lead to more sensitivity to speed changes, as shown in Supplementary Figs. 7A–B. Lower cutoff frequencies lead to increased sensitivity to motion artifacts, which typically cause incomplete rejection of static signal and therefore, overestimation of the dynamic signal. Epochs with severe motion artifacts were discarded. The dRBC content metric, as computed here, is minimally sensitive to speed within a physiological range and has a time-course similar to hemoglobin changes (Fig. 3). If the average over the sliding window of width $2\Delta T = 252$ ms is approximated as the expectation, denoted by $E[\cdot]$, then the dynamic signal intensity is approximately equal to the expected value of the squared norm of the dynamic signal.

Likewise, the static signal intensity is estimated as shown below.

$$I_s(x,z,T)=\sum_{t=T-\Delta T}^{T+\Delta T}\left|A(x,z,t)*[\delta(t)-h(t)]\right|^2-\sum_{t=T-\Delta T}^{T+\Delta T}\left|A_{bckgnd}(z,t)*[\delta(t)-h(t)]\right|^2\cong E\left[\left|A_s(x,z,T)\right|^2\right]$$

The convolution kernel $\delta(t)-h(t)$, where $\delta(t)$ is the Dirac delta function, has frequency response 1-H(f). Motion correction was performed on all frames prior to convolution. The bias due to noise was corrected by applying an identical filter to a background region of the image and subtracting the result, as shown above. If the average over the sliding window is approximated as the expectation, denoted by $E[\cdot]$, then the static intensity is approximately equal to the expected value of the squared norm of the static signal.

We used models developed earlier (Radhakrishnan and Srinivasan, 2013) to interpret static and dynamic signal intensities (I_s and I_d, respectively). Critically, both the static and dynamic signals were assumed to experience the same attenuation coefficient $\mu_t(z,T)$, which was allowed to vary with cortical depth and time, while the static backscattering $B_s(z)$ was assumed to remain constant during activation. Dynamic backscattering $B_d(z,T)$ was allowed to change due to increases in RBC density and potentially orientation changes (Note that here, dynamic backscattering may include photons forward scattered by a red blood cell and subsequently backscattered from tissue). We also define signals integrated over slabs centered at z_0 (assuming the slab height, 2dz, is sufficiently thin):

$$\bar{I}_s(z_0,T)=\int_{z_0-dz}^{z_0+dz}\int_x I_s(x,z,T)dxdz\approx B_s(z_0)g(z_0)\exp\left[-2\int_0^{z_0}\mu_t(z,T)dz\right]$$

$$\bar{I}_d(z_0,T)=\int_{z_0-dz}^{z_0+dz}\int_x I_d(x,z,T)dxdz\approx B_d(z_0,T)g(z_0)\exp\left[-2\int_0^{z_0}\mu_t(z,T)dz\right].$$

In the expressions above, g(z) is a "catchall" term related to the spectrometer roll-off and depth of focus. Defining a dynamic signal metric based on $\bar{I}_d$ alone has the disadvantage that increases in μ_t (caused by more attenuation from increased scattering) confounds depth-specificity since an increase in μ_t leads to depth-dependent decreases in all detected signal, static or dynamic. Therefore, a normalization procedure ($\bar{I}_{norm}=\bar{I}_d\,/\,\bar{I}_s$) was employed to achieve depth-specificity and account for the potentially confounding effects of attenuation changes (Radhakrishnan and Srinivasan, 2013).

$$\bar{I}_{norm}(z_0,T)=\frac{\bar{I}_d(z_0,T)}{\bar{I}_s(z_0,T)}=\frac{B_d(z_0,T)}{B_s(z_0)}$$

Moreover, by considering relative changes during activation, and assuming no changes in static backscattering, we obtain:

$$\frac{\Delta\bar{I}_{norm}(z_0,T)}{\bar{I}_{norm}(z_0,0)}=\frac{\Delta B_d(z_0,T)}{B_d(z_0,0)}$$

Thus by normalizing the dynamic to the static signal, a depth-specific metric of changes in dynamic backscattering is achieved. The time courses for $\Delta\bar{I}_s/\bar{I}_s$, $\Delta\bar{I}_d/\bar{I}_d$, and $\Delta\bar{I}_{norm}/\bar{I}_{norm}$ are shown in Supplementary Fig. 8, where intensities $\bar{I}_d$ and $\bar{I}_s$ were obtained by averaging over 100 μm slabs at different cortical depths, excluding regions with pial vasculature, to generate laminar profiles. As blood scattering is predominantly from red blood cells and, furthermore, our technique detects only moving red blood cells, we attribute relative changes in the normalized dynamic scattering ($\Delta\bar{I}_{norm}/\bar{I}_{norm}$) to changes in "dynamic red blood cell (RBC) content" (Radhakrishnan and Srinivasan, 2013). Further validation of this method with blood flow phantoms is presented in Supplementary Fig. 3.

A.2. Bandwidth and red blood cell speed

The bandwidth of the dynamic signal component was interpreted as being proportional to RBC speed. Briefly, the dynamic component of the autocorrelation was estimated as follows (Srinivasan et al., 2012b):

$$R_d(x,z,\tau,T)=\frac{\Delta t}{2\Delta T-\tau+\Delta t}\sum_{t=T-\Delta T+\tau/2}^{T+\Delta T-\tau/2}A(x,z,t+\tau/2)\bar{A}(x,z,t-\tau/2)-I_s(x,z,T)$$

In the above expression, Δt is the interframe time of 7 ms and τ represents the autocorrelation lag, determined up to a maximum time of 63 ms. From this estimate, we determined the bandwidth as a function of time by taking a discrete Fourier transform (DFT) with respect to the variable τ:

$$BW(x,z,T)=\frac{\sum_f|f|\times DFT_\tau[|R_d(x,z,\tau,T)|]}{\sum_f DFT_\tau[|R_d(x,z,\tau,T)|]}.$$

We note here that due to the in vivo sampling rate of $\Delta t=7$ ms, the autocorrelation is estimated at this interval, and the bandwidth is susceptible to aliasing effects which may lead to underestimates in the magnitude of relative changes. Additionally, although static scattering was accounted for, neither additive nor multiplicative noise bias was corrected in the autocorrelation. Hence we do not explicitly interpret the *magnitude* of relative changes in the bandwidth in this work, and only interpret the *kinetics* of the relative changes in bandwidth. Lastly, we note that motion artifacts lead to incomplete rejection of static signal and therefore, underestimation of the bandwidth. Epochs with severe motion artifacts were discarded. Further validation of this method in flow phantoms is presented in Supplementary Fig. 3.

A.3. Attenuation coefficient changes and red blood cell content

By taking the logarithm of the relative static signal over time, it is possible to determine changes in the attenuation coefficient.

$$\log\left[\frac{\bar{I}_s(z_0,T)}{\bar{I}_s(z_0,0)}\right]=-2\int_0^{z_0}[\mu_t(z,T)-\mu_t(z,0)]dz=-2\int_0^{z_0}\Delta\mu_t(z,T)dz$$

By taking the derivative of both sides with respect to z_0, we obtain the following expression.

$$\frac{d}{dz_0}\left\{\log\left[\frac{\bar{I}_s(z_0,T)}{\bar{I}_s(z_0,0)}\right]\right\}=-2\Delta\mu_t(z_0,T)$$

Simplifying further, for small changes in static scattering we obtain the following expression:

$$\Delta\mu_t(z_0,T)=-\frac{1}{2}\frac{d}{dz_0}\left\{\Delta\log\left[\bar{I}_s(z_0,T)\right]\right\}$$

In Supplementary Fig. 4, the depth-dependent change in attenuation coefficient is used to characterize the laminar hemodynamic response. We note here that *un-normalized changes* in the attenuation coefficient (assumed to indicate changes in RBC number per unit cortical volume, irrespective of the baseline values) can be readily determined from functional measurements. *Baseline-normalized changes* require knowledge of baseline attenuation due to RBC scattering, which can be challenging to determine due to the presence of tissue scattering, spectrometer roll-off, and Gaussian beam focusing effects. A similar phenomenon is observed in continuous wave functional near-infrared spectroscopy: absolute values require careful instrumental calibration, whereas changes during functional activation can be obtained without such calibration. The fact that the attenuation coefficient increases more in layer IV implies that the RBC number per unit cortical volume increases more during activation in layer IV than in other cortical layers. However, this fact alone does not necessarily imply that the changes in microvascular RBC *linear density* are the highest in layer IV, as microvascular density varies across layers, and is highest in layer IV (Blinder et al., 2013). The attenuation coefficient data interpretation is also potentially confounded by the fact that multiply scattered light becomes more significant in deeper cortical layers.

Appendix B. Supplementary data

Supplementary data to this article can be found online at http://dx.doi.org/10.1016/j.neuroimage.2014.08.004.

References

Avermann, M., Tomm, C., Mateo, C., Gerstner, W., Petersen, C.C., 2012. Microcircuits of excitatory and inhibitory neurons in layer 2/3 of mouse barrel cortex. J. Neurophysiol. 107, 3116–3134.

Blinder, P., Tsai, P.S., Kaufhold, J.P., Knutsen, P.M., Suhl, H., Kleinfeld, D., 2013. The cortical angiome: an interconnected vascular network with noncolumnar patterns of blood flow. Nat. Neurosci. 16, 889–897.

Buxton, R.B., 2001. The elusive initial dip. Neuroimage 13, 953–958.

Cauli, B., Tong, X.K., Rancillac, A., Serluca, N., Lambolez, B., Rossier, J., Hamel, E., 2004. Cortical GABA interneurons in neurovascular coupling: relays for subcortical vasoactive pathways. J. Neurosci. 24, 8940–8949.

Chaigneau, E., Oheim, M., Audinat, E., Charpak, S., 2003. Two-photon imaging of capillary blood flow in olfactory bulb glomeruli. Proc. Natl. Acad. Sci. U. S. A. 100, 13081–13086.

Chen, J.J., Pike, G.B., 2009. Origins of the BOLD post-stimulus undershoot. Neuroimage 46, 559–568.

Chen, Y., Aguirre, A.D., Ruvinskaya, L., Devor, A., Boas, D.A., Fujimoto, J.G., 2008. Optical coherence tomography (OCT) reveals depth-resolved dynamics during functional brain activation. J. Neurosci. Methods 178, 162–173.

Chen, B.R., Bouchard, M.B., McCaslin, A.F.H., Burgess, S.A., Hillman, E.M.C., 2011. High-speed vascular dynamics of the hemodynamic response. Neuroimage 54, 1021–1030.

Chmielowska, J., Kossut, M., Chmielowski, M., 1986. Single vibrissal cortical column in the mouse labeled with 2-deoxyglucose. Exp. Brain Res. 63, 607–619.

Dale, A.M., 1999. Optimal experimental design for event related fMRI. Hum. Brain Mapp. 8, 109–114.

Drew, P.J., Shih, A.Y., Kleinfeld, D., 2011. Fluctuating and sensory-induced vasodynamics in rodent cortex extend arteriole capacity. Proc. Natl. Acad. Sci. U. S. A. 108, 8473–8478.

Dunn, A.K., Devor, A., Dale, A.M., Boas, D.A., 2005. Spatial extent of oxygen metabolism and hemodynamic changes during functional activation of the rat somatosensory cortex. Neuroimage 27, 279–290.

Einevoll, G.T., Pettersen, K.H., Devor, A., Ulbert, I., Halgren, E., Dale, A.M., 2007. Laminar population analysis: estimating firing rates and evoked synaptic activity from multielectrode recordings in rat barrel cortex. J. Neurophysiol. 97, 2174–2190.

Fabricius, M., Akgoren, N., Dirnagl, U., Lauritzen, M., 1997. Laminar analysis of cerebral blood flow in cortex of rats by laser-Doppler flowmetry: a pilot study. J. Cereb. Blood Flow Metab. 17, 1326–1336.

Fingler, J., Schwartz, D., Yang, C., Fraser, S.E., 2007. Mobility and transverse flow visualization using phase variance contrast with spectral domain optical coherence tomography. Opt. Express 15, 12636–12653.

Franceschini, M.A., Nissila, I., Wu, W., Diamond, S.G., Bonmassar, G., Boas, D.A., 2008. Coupling between somatosensory evoked potentials and hemodynamic response in the rat. Neuroimage 41, 189–203.

Frostig, R.D., Lieke, E.E., Ts'o, D.Y., Grinvald, A., 1990. Cortical functional architecture and local coupling between neuronal activity and the microcirculation revealed by in vivo high-resolution optical imaging of intrinsic signals. Proc. Natl. Acad. Sci. U. S. A. 87, 6082–6086.

Goense, J.B., Logothetis, N.K., 2006. Laminar specificity in monkey V1 using high-resolution SE-fMRI. Magn. Reson. Imaging 24, 381–392.

Goense, J., Merkle, H., Logothetis, N.K., 2012. High-resolution fMRI reveals laminar differences in neurovascular coupling between positive and negative BOLD responses. Neuron 76, 629–639.

Harel, N., Lin, J., Moeller, S., Ugurbil, K., Yacoub, E., 2006. Combined imaging-histological study of cortical laminar specificity of fMRI signals. Neuroimage 29, 879–887.

Herman, P., Sanganahalli, B.G., Hyder, F., 2009. Multimodal measurements of blood plasma and red blood cell volumes during functional brain activation. J. Cereb. Blood Flow Metab. 29, 19–24.

Herman, P., Sanganahalli, B.G., Blumenfeld, H., Rothman, D.L., Hyder, F., 2013. Quantitative basis for neuroimaging of cortical laminae with calibrated functional MRI. Proc. Natl. Acad. Sci. U. S. A. 110, 15115–15120.

Hillman, E.M., Devor, A., Bouchard, M.B., Dunn, A.K., Krauss, G.W., Skoch, J., Bacskai, B.J., Dale, A.M., Boas, D.A., 2007. Depth-resolved optical imaging and microscopy of vascular compartment dynamics during somatosensory stimulation. Neuroimage 35, 89–104.

Horton, N.G., Wang, K., Kobat, D., Clark, C.G., Wise, F.W., Schaffer, C.B., Xu, C., 2013. Three-photon microscopy of subcortical structures within an intact mouse brain. Nat. Photonics 7.

Huang, D., Swanson, E.A., Lin, C.P., Schuman, J.S., Stinson, W.G., Chang, W., Hee, M.R., Flotte, T., Gregory, K., Puliafito, C.A., Fujimoto, J.G., 1991. Optical coherence tomography. Science 254, 1178–1181.

Izatt, J.A., Hee, M.R., Owen, G.M., Swanson, E.A., Fujimoto, J.G., 1994. Optical coherence microscopy in scattering media. Opt. Lett. 19, 590–592.

Jin, T., Kim, S.G., 2008. Cortical layer-dependent dynamic blood oxygenation, cerebral blood flow and cerebral blood volume responses during visual stimulation. Neuroimage 43, 1–9.

Kleinfeld, D., Mitra, P.P., Helmchen, F., Denk, W., 1998. Fluctuations and stimulus-induced changes in blood flow observed in individual capillaries in layers 2 through 4 of rat neocortex. Proc. Natl. Acad. Sci. U. S. A. 95, 15741–15746.

Kobat, D., Durst, M.E., Nishimura, N., Wong, A.W., Schaffer, C.B., Xu, C., 2009. Deep tissue multiphoton microscopy using longer wavelength excitation. Opt. Express 17, 13354–13364.

Kohl, M., Lindauer, U., Royl, G., Kuhl, M., Gold, L., Villringer, A., Dirnagl, U., 2000. Physical model for the spectroscopic analysis of cortical intrinsic optical signals. Phys. Med. Biol. 45, 3749–3764.

Kwong, K.K., Belliveau, J.W., Chesler, D.A., Goldberg, I.E., Weisskoff, R.M., Poncelet, B.P., Kennedy, D.N., Hoppel, B.E., Cohen, M.S., Turner, R., Cheng, H.-M., Brady, T.J., Rosen, B. R., 1992. Dynamic magnetic resonance imaging of human brain activity during primary sensory stimulation. Proc. Natl. Acad. Sci. U. S. A. 89, 5675–5679.

Lau, C., Zhou, I.Y., Cheung, M.M., Chan, K.C., Wu, E.X., 2011. BOLD temporal dynamics of rat superior colliculus and lateral geniculate nucleus following short duration visual stimulation. PLoS One 6, e18914.

Leitgeb, R., Hitzenberger, C.K., Fercher, A.F., 2003. Performance of Fourier domain vs. time domain optical coherence tomography. Opt. Express 11, 889–894.

Logothetis, N.K., 2008. What we can do and what we cannot do with fMRI. Nature 453, 869–878.

Logothetis, N., Merkle, H., Augath, M., Trinath, T., Ugurbil, K., 2002. Ultra high-resolution fMRI in monkeys with implanted RF coils. Neuron 35, 227–242.

Lu, H., Patel, S., Luo, F., Li, S.J., Hillard, C.J., Ward, B.D., Hyde, J.S., 2004. Spatial correlations of laminar BOLD and CBV responses to rat whisker stimulation with neuronal activity localized by Fos expression. Magn. Reson. Med. 52, 1060–1068.

Maheswari, R.U., Takaoka, H., Kadono, H., Homma, R., Tanifuji, M., 2003. Novel functional imaging technique from brain surface with optical coherence tomography enabling visualization of depth resolved functional structure in vivo. J. Neurosci. Methods 124, 83–92.

Malonek, D., Dirnagl, U., Lindauer, U., Yamada, K., Kanno, I., Grinvald, A., 1997. Vascular imprints of neuronal activity: relationships between the dynamics of cortical blood flow, oxygenation, and volume changes following sensory stimulation. Proc. Natl. Acad. Sci. U. S. A. 94, 14826–14831.

Mandeville, J.B., Marota, J.J., 1999. Vascular filters of functional MRI: spatial localization using BOLD and CBV contrast. Magn. Reson. Med. 42, 591–598.

Mandeville, J.B., Marota, J.J.A., Kosofsky, B.E., Keltner, J.R., Weissleder, R., Rosen, B.R., Weisskoff, R.M., 1998. Dynamic functional imaging of relative cerebral blood volume during rat forepaw stimulation. Magn. Reson. Med. 39, 615–624.

Mandeville, J.B., Marota, J.J., Ayata, C., Moskowitz, M.A., Weisskoff, R.M., Rosen, B.R., 1999. MRI measurement of the temporal evolution of relative CMRO(2) during rat forepaw stimulation. Magn. Reson. Med. 42, 944–951.

Mariampillai, A., Standish, B.A., Moriyama, E.H., Khurana, M., Munce, N.R., Leung, M.K.K., Jiang, J.Y., Cable, A.E., Wilson, B.C., Vitkin, I.A., Yang, V.X.D., 2008. Speckle variance detection of microvasculature using swept-source optical coherence tomography. Opt. Lett. 33, 1530–1532.

Masamoto, K., Kanno, I., 2012. Anesthesia and the quantitative evaluation of neurovascular coupling. J. Cereb. Blood Flow Metab. 32, 1233–1247.

Masamoto, K., Kurachi, T., Takizawa, N., Kobayashi, H., Tanishita, K., 2004. Successive depth variations in microvascular distribution of rat somatosensory cortex. Brain Res. 995, 66–75.

Mayhew, J., Johnston, D., Berwick, J., Jones, M., Coffey, P., Zheng, Y., 2000. Spectroscopic analysis of neural activity in brain: increased oxygen consumption following activation of barrel cortex. Neuroimage 12, 664–675.

Nemoto, M., Sheth, S., Guiou, M., Pouratian, N., Chen, J.W., Toga, A.W., 2004. Functional signal- and paradigm-dependent linear relationships between synaptic activity and hemodynamic responses in rat somatosensory cortex. J. Neurosci. 24, 3850–3861.

Obata, T., Liu, T.T., Miller, K.L., Luh, W.M., Wong, E.C., Frank, L.R., Buxton, R.B., 2004. Discrepancies between BOLD and flow dynamics in primary and supplementary motor areas: application of the balloon model to the interpretation of BOLD transients. Neuroimage 21, 144–153.

Ogawa, S., Tank, D., Menon, R., Ellermann, J., Kim, S.-G., Merkel, H., Ugurbil, K., 1992. Intrinsic signal changes accompanying sensory stimulation: functional brain mapping with magnetic resonance imaging. Proc. Natl. Acad. Sci. U. S. A. 89, 5951–5955.

Radhakrishnan, H., Srinivasan, V.J., 2013. Compartment-resolved imaging of cortical functional hyperemia with OCT angiography. Biomed. Opt. Express 4, 1255–1268.

Raichle, M.E., Mintun, M.A., 2006. Brain work and brain imaging. Annu. Rev. Neurosci. 29, 449–476.

Ren, H., Du, C., Park, K., Volkow, N.D., Pan, Y., 2012. Quantitative imaging of red blood cell velocity invivo using optical coherence Doppler tomography. Appl. Phys. Lett. 100, 233702–2337024.

Shen, Q., Ren, H., Duong, T.Q., 2008. CBF, BOLD, CBV, and CMRO(2) fMRI signal temporal dynamics at 500-msec resolution. J. Magn. Reson. Imaging 27, 599–606.

Sheth, S.A., Nemoto, M., Guiou, M., Walker, M., Pouratian, N., Hageman, N., Toga, A.W., 2004. Columnar specificity of microvascular oxygenation and volume responses: implications for functional brain mapping. J. Neurosci. 24, 634–641.

Shih, Y.Y., Chen, Y.Y., Lai, H.Y., Kao, Y.C., Shyu, B.C., Duong, T.Q., 2013. Ultra high-resolution fMRI and electrophysiology of the rat primary somatosensory cortex. Neuroimage 73, 113–120.

Shmuel, A., Yacoub, E., Pfeuffer, J., Van de Moortele, P.F., Adriany, G., Hu, X., Ugurbil, K., 2002. Sustained negative BOLD, blood flow and oxygen consumption response and its coupling to the positive response in the human brain. Neuron 36, 1195–1210.

Siero, J.C., Petridou, N., Hoogduin, H., Luijten, P.R., Ramsey, N.F., 2011. Cortical depth-dependent temporal dynamics of the BOLD response in the human brain. J. Cereb. Blood Flow Metab. 31, 1999–2008.

Silva, A.C., Koretsky, A.P., 2002. Laminar specificity of functional MRI onset times during somatosensory stimulation in rat. Proc. Natl. Acad. Sci. U. S. A. 99, 15182–15187.

Smirnakis, S.M., Schmid, M.C., Weber, B., Tolias, A.S., Augath, M., Logothetis, N.K., 2007. Spatial specificity of BOLD versus cerebral blood volume fMRI for mapping cortical organization. J. Cereb. Blood Flow Metab. 27, 1248–1261.

Srinivasan, V.J., Radhakrishnan, H., Jiang, J.Y., Barry, S., Cable, A.E., 2012a. Optical coherence microscopy for deep tissue imaging of the cerebral cortex with intrinsic contrast. Opt. Express 20, 2220–2239.

Srinivasan, V.J., Radhakrishnan, H., Lo, E.H., Mandeville, E.T., Jiang, J.Y., Barry, S., Cable, A.E., 2012b. OCT methods for capillary velocimetry. Biomed. Opt. Express 3, 612–629.

Stefanovic, B., Hutchinson, E., Yakovleva, V., Schram, V., Russell, J.T., Belluscio, L., Koretsky, A.P., Silva, A.C., 2008. Functional reactivity of cerebral capillaries. J. Cereb. Blood Flow Metab. 28, 961–972.

Tao, Y.K., Davis, A.M., Izatt, J.A., 2008. Single-pass volumetric bidirectional blood flow imaging spectral domain optical coherence tomography using a modified Hilbert transform. Opt. Express 16, 12350–12361.

Tian, P., Teng, I.C., May, L.D., Kurz, R., Lu, K., Scadeng, M., Hillman, E.M.C., de Crespigny, A.J., D'Arceuil, H.E., Mandeville, J.B., Marota, J.J., Rosen, B.R., Liu, T.T., Boas, D.A., Buxton, R.B., Dale, A.M., Devor, A., 2010. Cortical depth-specific microvascular dilation underlies laminar differences in blood oxygenation level-dependent functional MRI signal. Proc. Natl. Acad. Sci. U. S. A. 107, 15246–15251.

Vakoc, B.J., Lanning, R.M., Tyrrell, J.A., Padera, T.P., Bartlett, L.A., Stylianopoulos, T., Munn, L.L., Tearney, G.J., Fukumura, D., Jain, R.K., Bouma, B.E., 2009. Three-dimensional microscopy of the tumor microenvironment in vivo using optical frequency domain imaging. Nat. Med. 15, 1219–1223.

Vanzetta, I., Hildesheim, R., Grinvald, A., 2005. Compartment-resolved imaging of activity-dependent dynamics of cortical blood volume and oximetry. J. Neurosci. 25, 2233–2244.

Wang, R.K., Jacques, S.L., Ma, Z., Hurst, S., Hanson, S.R., Gruber, A., 2007. Three dimensional optical angiography. Opt. Express 15, 4083–4097.

Winfield, D.A., Gatter, K.C., Powell, T.P., 1980. An electron microscopic study of the types and proportions of neurons in the cortex of the motor and visual areas of the cat and rat. Brain 103, 245–258.

Wong-Riley, M.T., 1989. Cytochrome oxidase: an endogenous metabolic marker for neuronal activity. Trends Neurosci. 12, 94–101.

Yacoub, E., Ugurbil, K., Harel, N., 2006. The spatial dependence of the poststimulus undershoot as revealed by high-resolution BOLD- and CBV-weighted fMRI. J. Cereb. Blood Flow Metab. 26, 634–644.

Yu, X., Glen, D., Wang, S., Dodd, S., Hirano, Y., Saad, Z., Reynolds, R., Silva, A.C., Koretsky, A.P., 2012. Direct imaging of macrovascular and microvascular contributions to BOLD fMRI in layers IV–V of the rat whisker-barrel cortex. Neuroimage 59, 1451–1460.

Yu, X., Qian, C., Chen, D.Y., Dodd, S.J., Koretsky, A.P., 2014. Deciphering laminar-specific neural inputs with line-scanning fMRI. Nat. Methods 11, 55–58.

Zhao, F., Wang, P., Hendrich, K., Ugurbil, K., Kim, S.G., 2006. Cortical layer-dependent BOLD and CBV responses measured by spin-echo and gradient-echo fMRI: insights into hemodynamic regulation. Neuroimage 30, 1149–1160.

Zhao, F., Jin, T., Wang, P., Kim, S.G., 2007. Improved spatial localization of post-stimulus BOLD undershoot relative to positive BOLD. Neuroimage 34, 1084–1092.